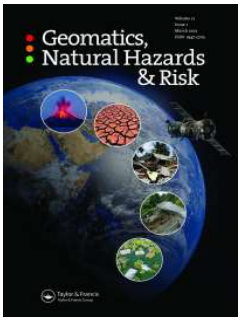

Geomatics, Natural Hazards and Risk

ISSN: (Print) (Online) Journal homepage: https://www.tandfonline.com/loi/tgnh20

Analyzing the formation mechanism of the Xuyong landslide, Sichuan province, China, and emergency monitoring based on multiple remote sensing platform techniques

Yi Luo, Wenliang Jiang, Bingquan Li, Qisong Jiao, Yongsheng Li, Qiang Li & Jingfa Zhang

To cite this article: Yi Luo, Wenliang Jiang, Bingquan Li, Qisong Jiao, Yongsheng Li, Qiang Li & Jingfa Zhang (2020) Analyzing the formation mechanism of the Xuyong landslide, Sichuan province, China, and emergency monitoring based on multiple remote sensing platform techniques, Geomatics, Natural Hazards and Risk, 11:1, 654-677, DOI: 10.1080/19475705.2020.1745903

To link to this article: https://doi.org/10.1080/19475705.2020.1745903

Published online: 08 Apr 2020.

GEOMATICS, NATURAL HAZARDS AND RISK
2020, VOL. 11, NO. 1, 654–677
https://doi.org/10.1080/19475705.2020.1745903

Analyzing the formation mechanism of the Xuyong landslide, Sichuan province, China, and emergency monitoring based on multiple remote sensing platform techniques

Yi Luo, Wenliang Jiang, Bingquan Li, Qisong Jiao, Yongsheng Li, Qiang Li and Jingfa Zhang

Institute of Crustal Dynamics, China Earthquake Administration, Beijing, China

ABSTRACT

In this study, multitemporal satellite images, unmanned aerial vehicle (UAV) photogrammetry and ground-based radar were utilized to investigate the formation mechanism and disaster features of different phases of the Xuyong landslide disaster that occurred in Sichuan Province on December 9, 2018. Field survey indicates that the estimated landslide volume is approximately 35000 m^3. The landslide is a typical dualistic soil-rock structural landslide with bedding planes. The sliding surface is located in a thin layer of limestone which is characterized by the X-shaped conjugate joint planes. The steep slope has been cut and transformed by human disturbances, which have influenced the slope stability and the drainage of precipitation along the slope. Many factors, including the regional geological structure, stratum lithology, slope topography, landform morphology, and precipitation, have contributed to the Xuyong landslide during the pre-disaster phase. Post-disaster emergency observation revealed that subsequent deformation was located mainly along the back edge of the landslide, where the maximum surficial deformation reached only 18 mm/day over a small area, reflecting the low probability of a secondary landslide hazard. Our research provides significant guidelines for investigating potential landslide dangers in similar environments and for post-disaster emergency response using multiple remote sensing (RS) platforms.

ARTICLE HISTORY
Received 9 January 2020
Accepted 5 March 2020

KEYWORDS
Xuyong landslide; remote sensing; formation mechanism; post-disaster deformation; emergency response

1. Introduction

Among all the countries in the world, China exhibits some of the most serious geological hazards, of which there are many different types that are widely distributed. Unfortunately, accurately predicting and warning of geological hazards are challenging tasks (Chen et al. 2011). Many geological hazards occur beyond the geological

CONTACT Wenliang Jiang (jiang_wenliang@163.com)

dangers that have been discovered in advance. For example, the landslide that occurred on June 24, 2017, in Xinmo, Sichuan Province, killed more than 100 people (Yin et al. 2016; Fan et al. 2017; Dong et al. 2018), and the landslide that occurred on July 23, 2019, in Shuicheng County, Guiyang Province, killed dozens of people. Geological hazards may pose serious dangers to human beings, and the effects of geological hazard chains are becoming progressively prominent (Iverson 2000; Lacroix et al. 2015; Intrieri and Gigli 2016; Pour and Hashim 2017; Hashim et al. 2018; Alizadeh et al. 2018a, 2018b, 2018c). In addition, geological hazards caused by engineering construction also occur frequently (Li et al. 2010; Sun et al. 2013; Smith et al. 2018); for example, the landslide disaster that occurred in Shenzhen on December 20, 2015, is believed to have been related to the artificial deposition of construction waste (Yin et al. 2016).

Accordingly, it is necessary to study the formation mechanisms and influencing factors, including the regional topography, geological structure, precipitation, and so on, of landslides that have already occurred to understand their evolutionary processes (Petley 2004; Take et al. 2004). This will enable the identification of potential landslide dangers in situations similar to those of landslides that have already occurred (Intrieri and Gigli 2016; Yan et al. 2019). However, in the landslide research that has been conducted, researchers have tended to miss important details in observations of post-disaster events, leading to an inability to predict the future development of such occurrences, which may have a cascading effect. For example, a secondary landslide disaster occurred on April 23, 2013, on the Qinggang slope in Sinan, Guizhou Province, resulting in 11 deaths. Another secondary landslide disaster occurred on July 1, 2017, in Ningxiang County, Hunan Province, causing 8 deaths and 19 injuries. These incidents reflect the importance of emergency monitoring schemes for geological hazards in the prevention of possible secondary disasters and in ensuring the safety of emergency responses. Therefore, it is very important to study different phases of landslides, including early identification, influencing factors and formation mechanism during the pre-disaster phase; disaster features during the landslides; and emergency monitoring in case of secondary disasters during the post-disaster phase. All these investigations will provide the foundation for the early identification and warning of major landslide events.

Photogrammetry and remote sensing (RS) have become important techniques in investigating geological dangers. By jointly analyzing the regional topography, geological structure and meteorological precipitation conditions, we can achieve the early identification of geological hazards. Both interferometric synthetic aperture radar (InSAR) (Hilley et al. 2004; Calabro et al. 2010; Dong et al. 2018) and optical image correlation techniques (Delacourt et al. 2004; Debella-Gilo and Kaab 2012; Stumpf et al. 2014, 2017) have been widely used to detect the deformation of slow-moving landslides. For the post-disaster emergency observation, ground-based radar can measure landslide deformation over a long distance (Pieraccini et al. 2003; Tarchi et al. 2003a, 2003b; Antonello et al. 2004; Noferini et al. 2007). In particular, post-disaster observations can reveal the development trend of landslide deformation, thereby providing emergency response personnel the opportunity to prevent a subsequent secondary disaster (Nikolakopoulos and Koukouvelas 2017; Del Ventisette et al. 2011).

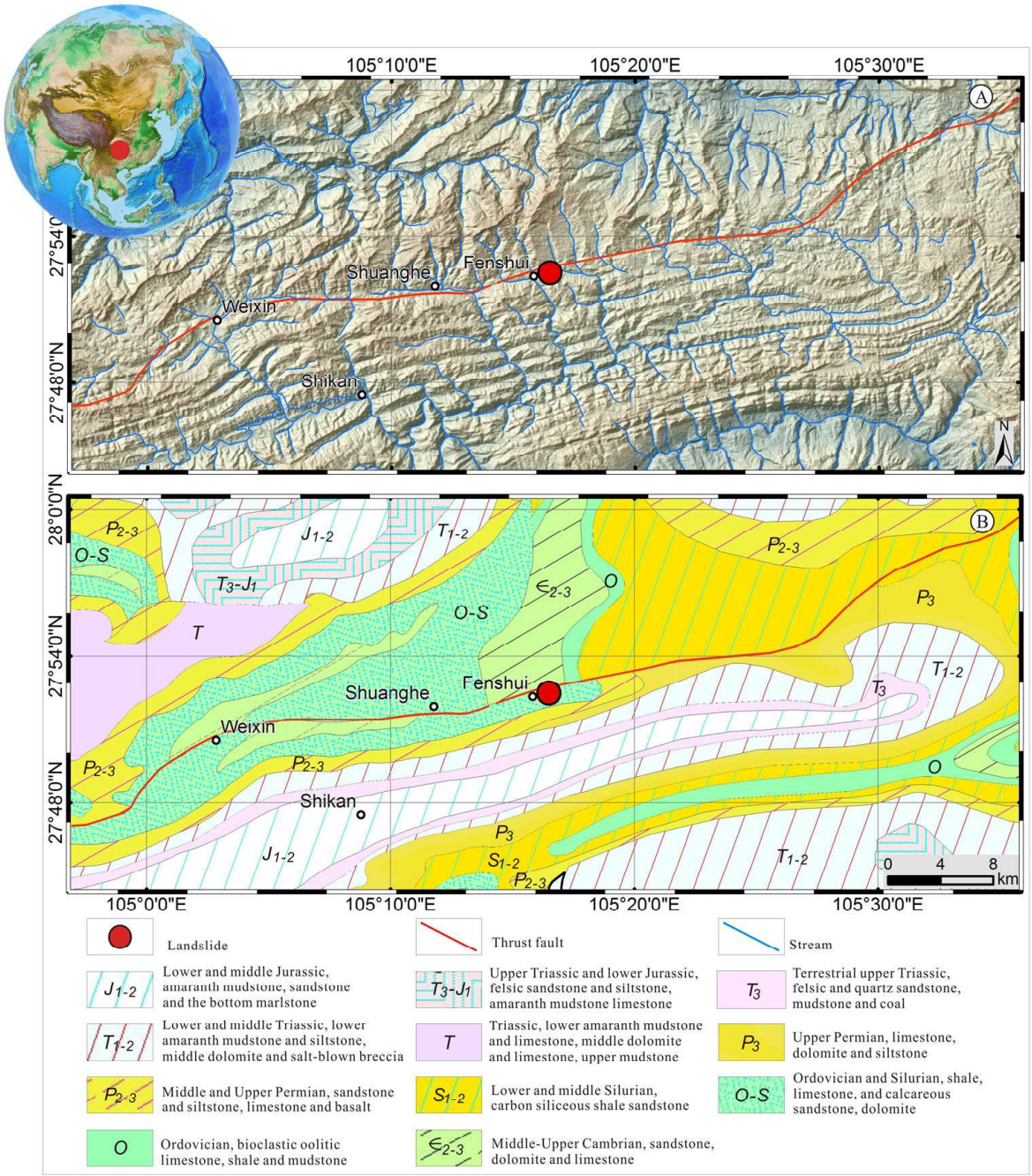

Figure 1. (a) Regional hillshade map with the hydrography of the area surrounding the Xuyong landslide, which occurred on December 9, 2018. An ASTER GDEM hillshade map is used as the base map. (b) Regional geological setting surrounding the Xuyong landslide (China geological survey 2014). The red line denotes active faults in this region (Modified from Deng et al. 2002).

Therefore, it is of considerable significance to identify major geological hazards as early as possible, to monitor and make early warnings of geological hazards, and to implement post-disaster emergency monitoring schemes using multiplatform RS techniques (Liu 2006; Canuti et al. 2007; Chen et al. 2011; Casagli et al. 2017).

On December 9, 2018, a landslide disaster occurred in the village of Fenshui, Xuyong County, Sichuan Province (Figure 1 and Figure 2), causing 5 deaths. To study the mechanism of the Xuyong landslide and to ensure the security of emergency response

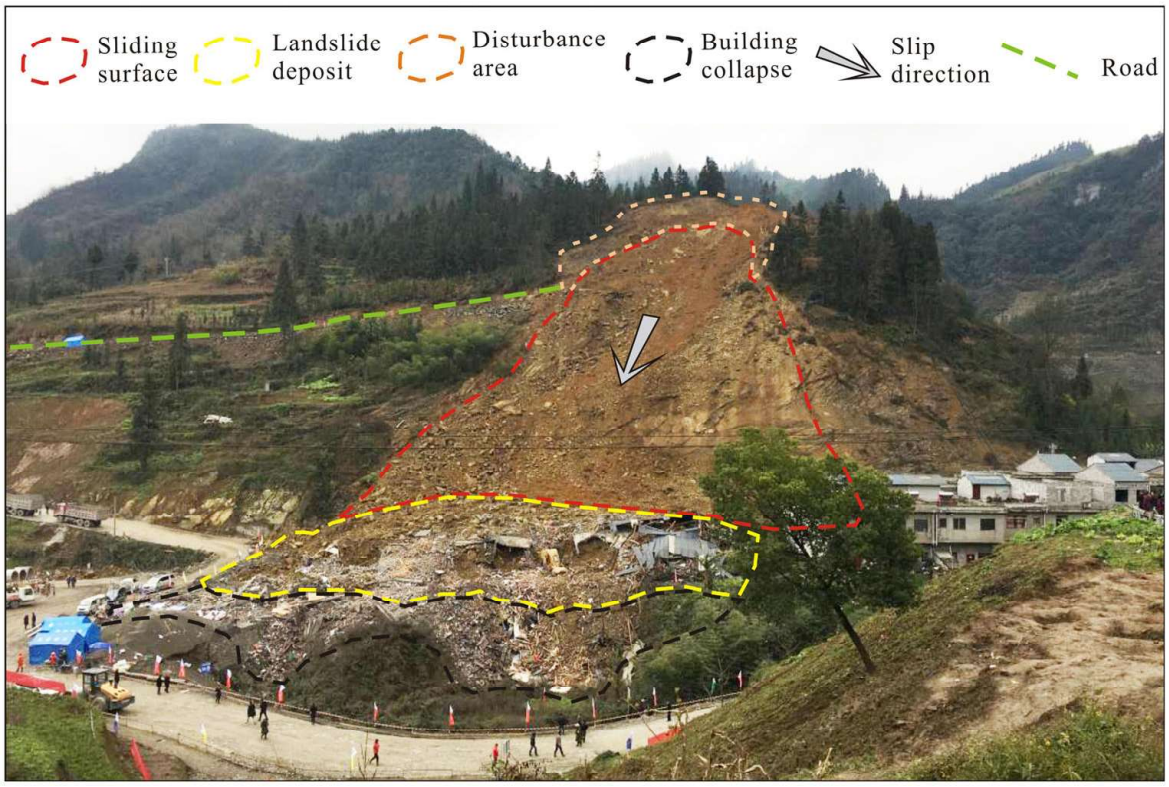

Figure 2. Field scenery of the Xuyong landslide disaster. The photograph was taken towards south. The red dashed line denotes the landslide bed. The yellow dashed line denotes the landslide deposition area. The black line denotes the building collapse destroyed by the landslide deposits. The sand yellow dashed line denotes the landform transforming region before the Xuyong landslide. The green dashed line denotes the road cut in the slope before the landslide. The hollow arrow reflects the sliding direction of the landslide.

endeavors, we used satellite images, unmanned aerial vehicle (UAV) photogrammetry and ground-based radar to analyze the landslide characteristics and observe the post-disaster deformation. In combination with analyses of the regional topography, geological structure and human disturbances, the formation process and mechanism of hidden landslide dangers were studied. This research is significant in that it provides reference information for the investigation and prevention of possible geological dangers in environments similar to that of the Xuyong landslide. Our research will also provide guidance for the investigation of landslide disasters using different RS platforms, including satellites, aerial photogrammetry and ground-based radar.

2. Study area description

The study area, which is subordinate to the city of Luzhou in Sichuan Province, is a low- to mid-altitude mountainous area located in the gradient zone of the southern Sichuan Basin (between the Sichuan Basin and the Yunnan-Guizhou Plateau, see Figure 1b) (National Geological Archives of China 2013). Influenced by the Neocathaysian structural system, the stress field of this area is very complicated and has produced a series of strong deformation zones that strike nearly E-W (Zhao et al. 2015). Accordingly, the geological structures in this region are very complicated with extremely diverse fold structures and crisscrossing faults. The Xuyong landslide is

located within the Weixin fold area, which is characterized by compact and nearly E-W- to ENE-WSW- trending linear folds (Liang et al. 2011). The anticlines in this area are composed mostly of lower Paleozoic rocks; many faults have developed along the axes and limbs of these anticlines, and the strata along the axes are steep and tilted. In contrast, the synclines comprise primarily upper Paleozoic and Mesozoic rocks; the strata on both limbs of the synclines exhibit steep dips, while those along the axes display gentle dips.

The strata in the study area are fully exposed in outcrops, from which it is known that the lithological characteristics differ markedly among the strata. Strata with ages ranging from the Quaternary to the Cambrian are observed in outcrops, and missing Tertiary and Carboniferous strata correspond to unconformities (National Geological Archives of China 2013). There is an unconformity between the Quaternary strata and the underlying strata, while the other strata present conformable or pseudoconformable contacts. The rocks of this region are highly fractured, and the local nonsoluble rocks are weakened. Therefore, some regions are prone to the formation of highly concentrated karst systems (Zhao et al. 2015). Triassic and Cambrian strata crop out more commonly than other strata, and the strata increase in age from north to south. Additionally, as observed from the variations in the structural traces throughout the study area, folding and faulting have intensively fractured the strata (complicating them greatly) under the NW-SE-striking stress (Deng 1965).

The Xuyong area is characterized by a subtropical humid monsoon climate. According to the China meteorological data, the average annual rainfall in Xuyong is approximately 1000 mm, and the average annual number of rainfall days is almost 200. Therefore, excessive rainfall in the Xuyong area may influence the topographic conditions and may trigger geological hazards.

Geological hazards, including landslides, rock avalanches, mud-rock flows, unstable slopes, ground collapses and ground fissures, occur frequently in Xuyong County, Sichuan Province. According to incomplete records, there are more than 130 hidden geological dangers in Xuyong County, including more than 110 landslide dangers and nearly 10 rock avalanche dangers. Although most of these geological hazards are medium to small in scale, they still pose great threats to this region. For example, on July 12, 2010, a small landslide with a volume of approximately 5000 m^3 occurred in Longfeng town in Xuyong, causing 6 deaths. On May 4, 2014, another landslide with a volume of approximately 10000 m^3 occurred in the Baihua village in Xuyong. Fortunately, there were no casualties because of immediate early warning and evacuation of the populace before the landslide. Both of these two landslides occurred during the rainfall season. However, the Xuyong landslide studied in this paper occurred without heavy rainfall on December 9, 2018.

3. Data and methods

3.1. Landslide danger and disaster monitoring

In this study, multitemporal satellite images acquired by the PlanetLabs' PlanetScope (PS) Earth-Imager, a multispectral CubeSats constellation, before the landslide occurred and UAV data captured immediately after the disaster are used to

Table 1. Satellite parameters of the PlanetScope imagery (Shi et al. 2018).

Parameters	Information
Orbit altitude	Sun-synchronous Orbit 475km
Orbit inclination	98°
Latitude coverage	81.5°N-81.5°S
Revisiting period	1 Day
Wave bands	Blue: 455-515nm; Green: 500-590nm; Red: 590-670nm; NIR: 780-860nm
Ground resolution	3m
Imagery Width	24.6 km x 16.4 km
Starting time	Since Sep. 2015

dynamically analyze the landslide hazard and disaster information. The PS CubeSats capture imagery at a ground sampling distance of 3.7 m at a reference altitude of 475 km, and the imagery is then orthorectified to a pixel size of 3 m (Table 1) (Shi et al. 2018). The multitemporal images acquired in this study were captured between 2018 and 2019 (Table 2, Figure 3). To match these multitemporal images, ground control points (GCPs) were selected with a uniform distribution manually in the images according to the imagery textures, such as buildings, roads and mountains. In addition, two Google-Earth images captured on December 12, 2017 (before the Xuyong landslide), and on March 3, 2019 (after the Xuyong landslide), are also collected for general comparisons (Figure 4). Based on these multitemporal images we can dynamically analyze the characteristics of the changes that occurred before the landslide by visual inspection. In particular, the anthropogenic alterations and topographic changes that result in human-induced landslide disasters can be visually identified directly, which is beneficial for understanding the formation mechanism of landslides.

After the Xuyong landslide disaster, stereoscopic orthographic images of the landslide were immediately acquired by a UAV manufactured by the DJI Enterprise of China. The take-off elevation of the UAV was approximately 1273 m, and the relative altitude was 200 m. In total, 72 orthographic stereoscopic images covering a total area of 0.13 km^2 were captured. During the field survey, we measured the coordinates of 3 points around the landslide as the GCPs for the UAV orthophoto images. The Pix4Dmapper procedure was used in this study to process the UAV images. Using these stereoscopic UAV images, the position and orientation system (POS) data of the UAV during flight and the GCPs, we obtained point data, a digital surface model (DSM) and a digital orthophoto map (DOM) after applying point data classification, texture processing, orthophoto processing and contour line generation. The vertical accuracy of the point data is approximately 15 cm and the ground resolution of the DSM is approximately 5 cm.

3.2. Deformation data acquisition and processing

A ground-based radar interferometry device was used to make emergency observations to detect post-disaster deformation of the Xuyong landslide. Ground-based radar can monitor deformation at a distance of tens to thousands of meters, and it can be used to define adequate prevention measures and to manage landslide emergencies (Casagli et al. 2010; Atzeni et al. 2015). Ground-based interferometric

Table 2. Dates of the multitemporal images.

Satellite	Figure number	Date
Planet's PlanetScope CubeSat constellation	Figure 3a	02-17-2018
	Figure 3b	03-15-2018
	Figure 3c	04-16-2018
	Figure 3d	05-16-2018
	Figure 3e	06-07-2018
	Figure 3f	08-25-2018
	Figure 3g	10-31-2018
	Figure 3h	02-07-2019

observations provide complementary information to spaceborne InSAR and conventional geodetic surveying methods for emergency observations (Werner et al. 2012). Because of their advantageous portability and ability to perform continuous monitoring, ground-based radar interferometers can be easily applied to various scenarios of engineering deformation and to warning and forecasting of geological hazards. In this study, a GAMMA portable radar interferometer II (GPRI-II) produced in Italy was used. It works in the Ku band with a microwave frequency of 17.2 GHz, a wavelength of 0.0176 m, and an effective measuring distance range of 0.05 to 10 km. Unlike ground-based synthetic aperture radar (SAR) sensors, the GPRI-II is a real aperture radar instrument. There are three antennas on the GPRI-II: one sends microwaves, while the other two receive echo signals (Figure 5). Because the spatial baseline is close to zero, the terrain phase can be minimized and even neglected. Also different from ground-based SAR equipment, which has a fixed observation direction, the GPRI-II can detect deformation in a 360-degree field in nearly real time. Therefore, the object deformation can be continuously monitored using the GPRI-II.

The range resolution of the GPRI-II is $\Delta d_{sr} = \frac{C}{2B}$, where C is the speed of light and B is the microwave bandwidth. As seen from the above equation, the range resolution is independent of the distance between the instrument and observation target. In addition, the azimuthal resolution of the GPRI-II is written as $\Delta d_{az} = sin(\theta_{-3dB}) \cdot R$, where θ_{-3dB} is the half-power wave velocity width, and R is the azimuthal distance.

To obtain high-quality data, the GPRI-II should be installed at a position with good viewing conditions, high foundation stability, and an appropriate angle between the line of sight (LOS) of the device and the main slip direction of the observed geological object. The observation parameters of the device, such as coherence threshold and time sampling interval, should be adjusted at the very start according to the environment and the quality of the observed data. The processing flow of the ground-based radar data mainly consists of four steps (Li et al., 2019), which include matching and pairing of interferometric data, differential interferometric processing, selection of characteristic points, and deformation analysis. The most frequently used methods for matching of interferometric data include persistent scatter interferometry (PSI) (Osmanoğlu et al., 2011), the stacking method (Wang et al. 2009), and nearest neighbor interference. The pairing strategy and time intervals for the combination of data pairs should be taken into consideration during the pairing step, as this influences the final results of the observed deformation. The differential interferograms that contain the atmospheric phase and deformation phase can be generated by differential interferometric processing according to the single look complex (SLC) data and

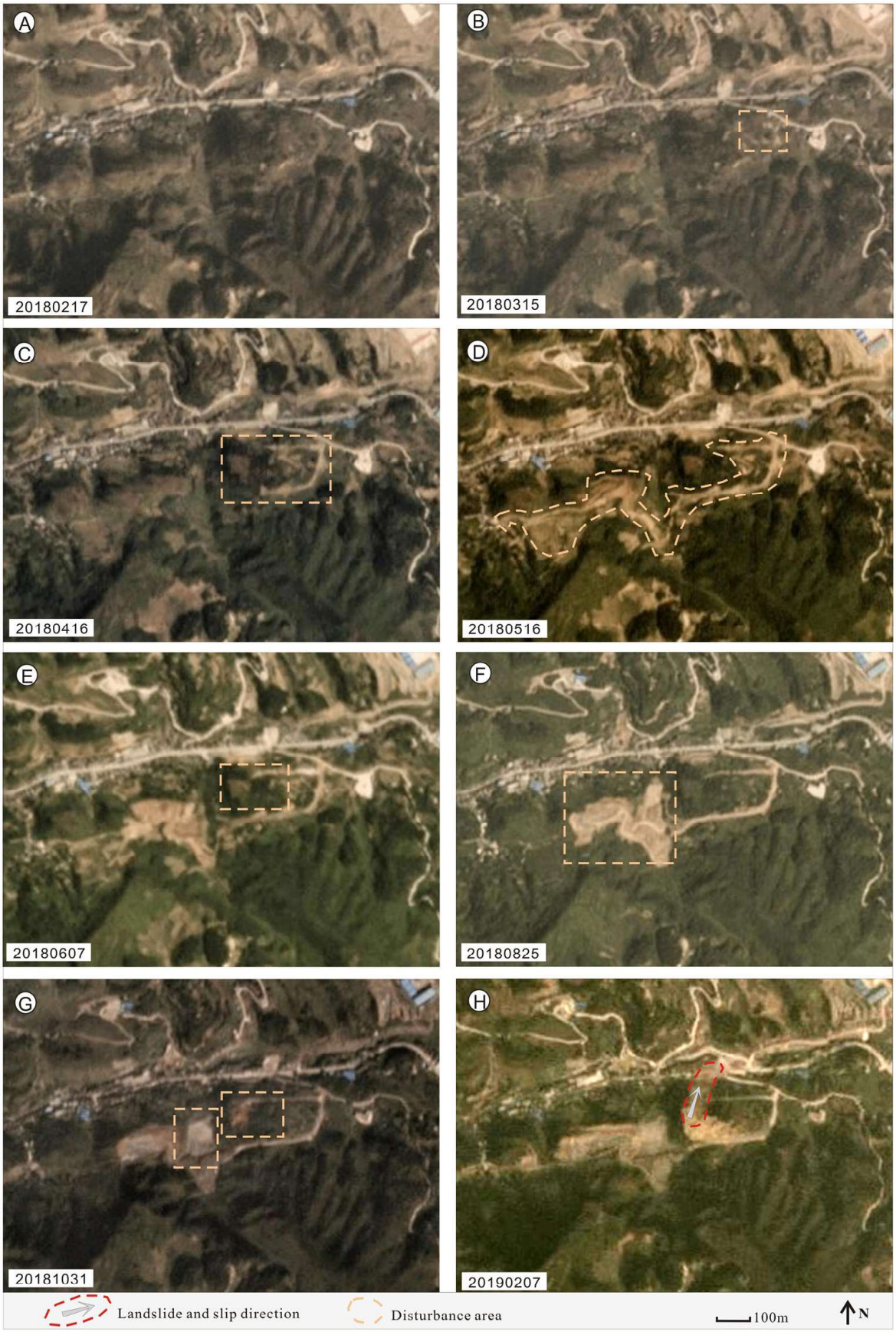

Figure 3. Multiple temporal images captured by the Planet's PlanetScope CubeSat constellation before and after the Xuyong landslide. The sand yellow dashed lines denote the landform transforming areas surrounding the landslide hidden danger. The red dashed line denotes the region of the landslide that occurred on December 9, 2018.

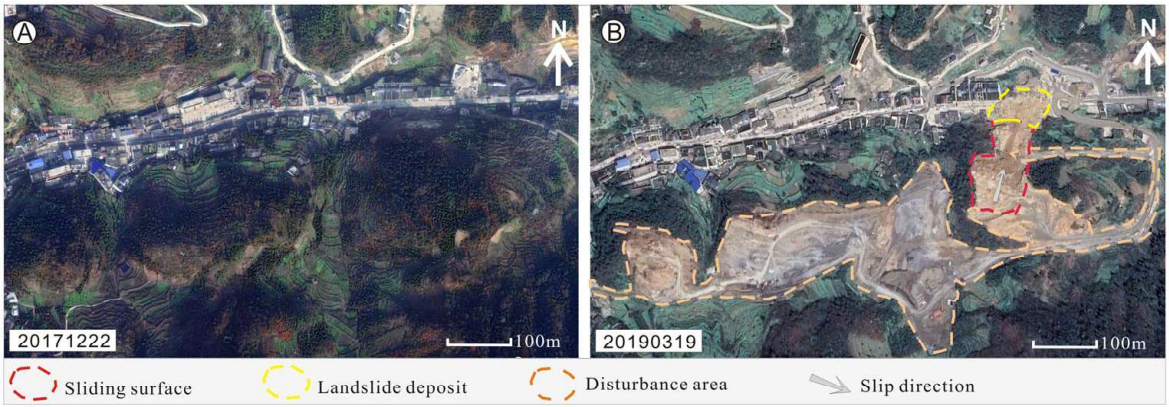

Figure 4. (a) The Google Earth image before the Xuyong landslide on December 12, 2017. (b) Google Earth image after the Xuyong landslide on March 3, 2019. The red dashed line denotes the landslide bed. The yellow dashed line denotes the landslide depositional area. The sand yellow dashed line denotes the landform transforming region before the Xuyong landslide. The hollow arrow reflects the sliding direction of the landslide.

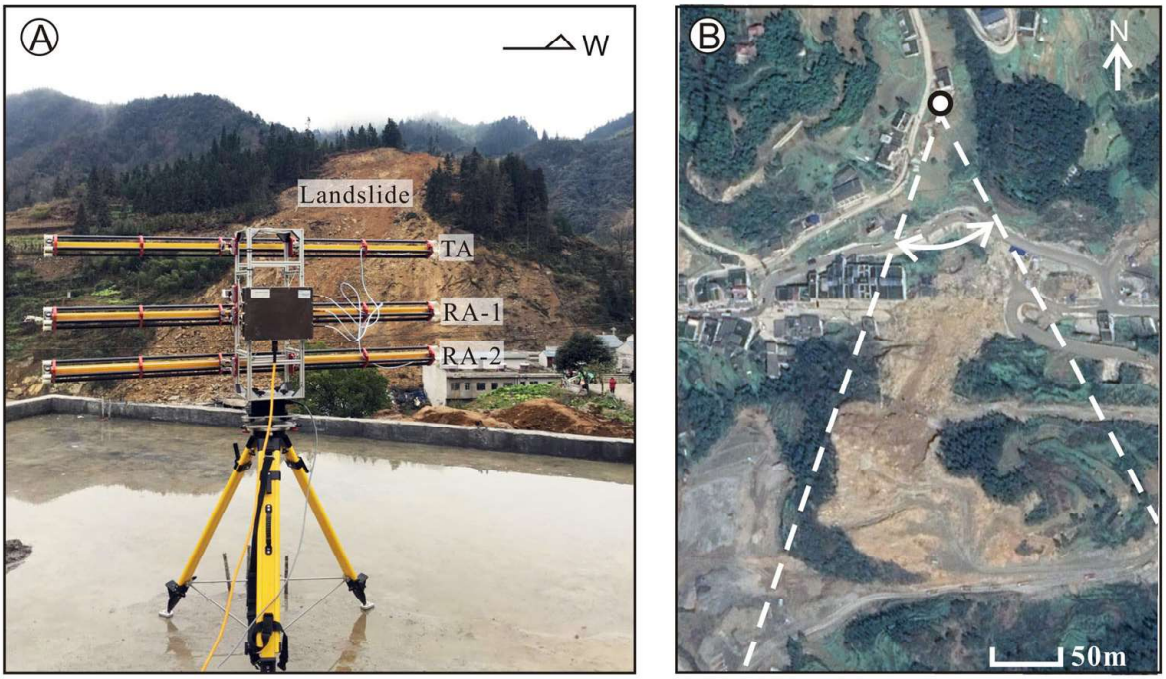

Figure 5. (a) Field work photos of the ground-based radar device for monitoring the post-disaster deformation, and the radar is employed in front of the Xuyong landslide. TA: Transmitting antenna. RA-1: 1st Receiving antenna. RA-2: 2nd Receiving antenna. (b) The white dot in the image show the location of the device equipped in from of the landslide. The dashed white lines denote the monitoring region by the device.

the interference pairing strategy. Consequently, the characteristic points with obvious deformation in the differential interferogram can be selected to determine the average deformation rate according to time-series analysis. The singular value decomposition (SVD) method (Li et al. 2013) is used to generate the time-series diagram of deformation. Through the time-series diagram of deformation, we can estimate deformation features of the landslide, including spatial distribution, deformation intensity, and future development trends, which can be used in the emergency response.

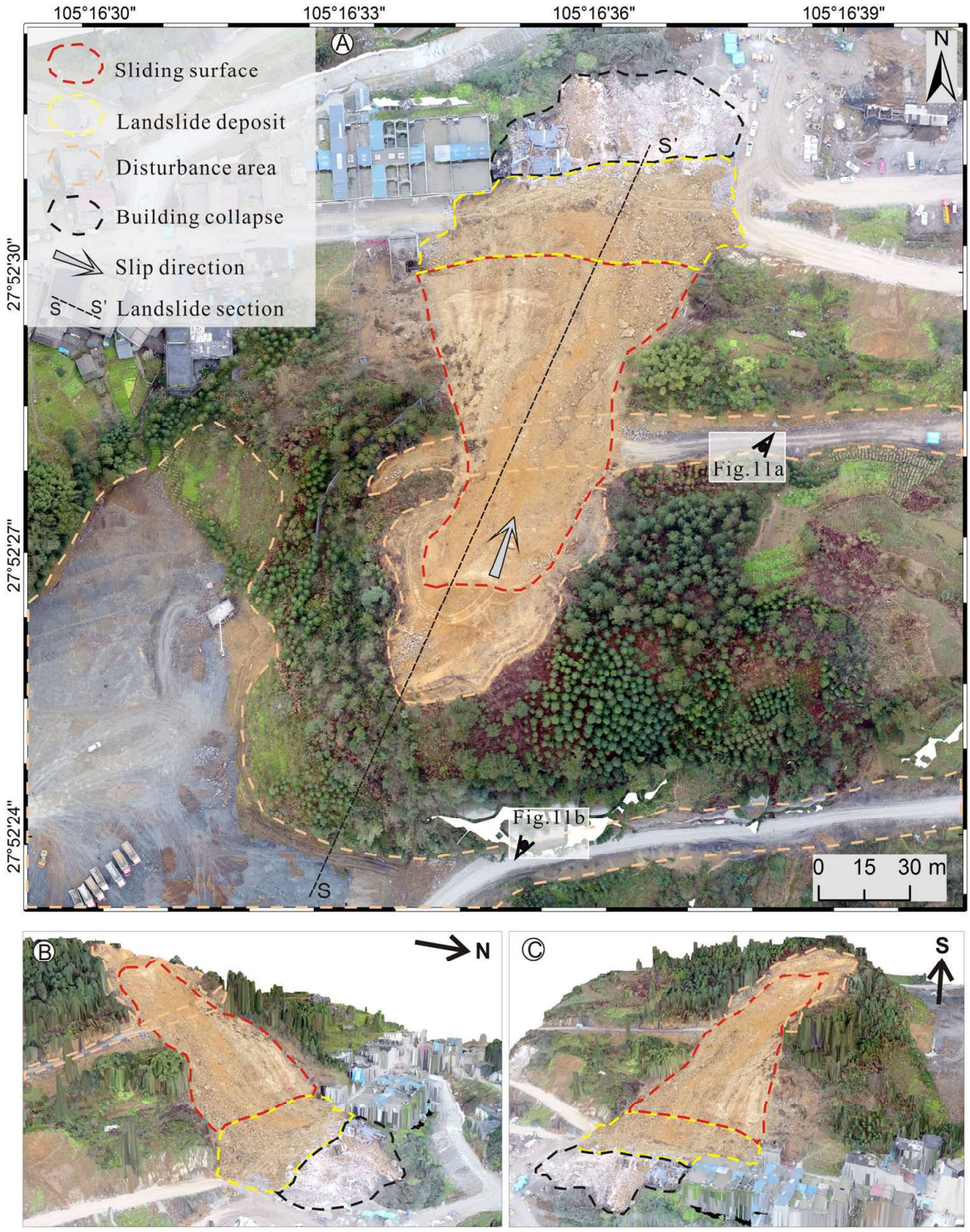

Figure 6. (a) Orthoimage of the Xuyong landslide disaster measured by the UAV method. Line SS′ denotes the section location of Figure 12. (b) and (c) are 3 D topographic scenes of the Xuyong landslide. Geomorphic classifications of landslide and artificial engineering regions are interpreted. The red dashed lines denote the landslide bed. The yellow dashed lines denote the landslide depositional area. The black lines denote the building collapse destroyed by the landslide deposits. The sand yellow dashed lines denote the landform transforming region before the Xuyong landslide. The hollow arrow reflects the sliding direction of the landslide.

The timing analysis of the ground-based GPRI-II is basically the same as that of spaceborne InSAR (Noferini et al. 2005). The largest difference is that the spatial

baseline of the ground-based radar is 0; therefore, image registration and terrain phase compensation are not needed during the processing of ground-based radar data. Consequently, the interferometric phase expression can be written as $\Delta\varphi = \varphi_{Defo}+\varphi_{Atmo}+\varphi_{Noise}+2k\pi$, where φ_{Defo} is the deformation phase, φ_{Atmo} is the atmospheric delay phase, and φ_{Noise} is the noise phase (Monserrat et al. 2014). During the post-disaster observation period, the range between the device and landslide was very suitable for radar observation; the distances between the device and the back margin and front edge of the landslide were approximately 330 m and 160 m. Additionally, the atmospheric delay phase can be eliminated by the high-pass filtering.

4. Landslide disaster and its formation process

According to the UAV images taken after the disaster occurred (Figure 6), we can accurately estimate the landslide and disaster information. The sliding direction of the landslide is 35°, and the landslide bed is approximately 140 m in length. The widths of the back and front margins of the landslide are approximately 40 m and 80 m, respectively. Furthermore, we can estimate that the total area of the landslide bed to be approximately 7000 m^2. According to the digital terrain model (DTM) obtained from the stereoscopic images, the undercutting depth of the landslide in cross section is approximately 4 to 6 m; therefore, the landslide is associated with a sediment volume of at least 35000 m^3. In addition, the length and width in the sliding direction are approximately 50 and 100 m, respectively; therefore, the depositional area is approximately 5000 m^2. According to the DTM, the thickness of the landslide deposit is approximately 4 to 7 m. Consequently, we can further estimate an accumulated sediment volume of approximately 35000 m^3. The two accumulated sediment volumes estimated according to the landslide bed and landslide deposit are consistent with each other.

Figure 4 shows a direct and considerable geomorphic contrast between the images taken in December 2017 and March 2019. A comparison of these two images reveals that large-scale topographic transformations occurred on the eastern, western, and southern sides of the Xuyong landslide (Figure 4b). In particular, the areas originally covered by vegetation (Figure 4a) transformed into bare surfaces. These transformations likely resulted from human disturbances around this region. An analysis of the multitemporal PS images also reveals multistage changes in the surface vegetation and landforms.

On the PS images of this region captured during different periods (Figure 3), we can observe many distinct topographic features changing with time. The satellite image from February 2018 (Figure 3a) indicates no differences in the topographic textures and grayscale features between the pre-disaster location of the landslide and the surrounding areas; in other words, the textural and grayscale features change naturally and uniformly. The initial change occurred in March 2018, when local textural changes appeared on the eastern side of the pre-disaster location of the Xuyong landslide (Figure 3b). Because the seasonal changes usually cause widespread changes in vegetation rather than a local change in this mountain area, therefore, we suppose

that these textural changes are related to human disturbance, which represents the initial landform transformation before the landslide. In the image captured on April 16, 2018 (Figure 3c), the topographic features of the pre-landslide area and the eastern part of the landslide clearly reveal changes. The most significant variation resulted from disturbances that occurred on the eastern side of the original site of the Xuyong landslide; as a consequence of these disturbances, a small (~50 m × ~50 m) area of vegetation appears in the original area of the landslide.

In the image from May 16, 2018 (Figure 3d), a large disturbance area of appears around the original site of the landslide disaster: an area of vegetation changed into an outcropp surface. The transformation during this period is the most obvious among the transformations evident in the other images. In the image acquired on June 7, 2018 (Figure 3e), the original slope was once again disturbed by human activity. In contrast, the original site of the landslide in the image from August 25, 2018 (Figure 3f), remains the same as before but has been influenced by the rainy season; vegetation is observable on the exposed soil, but disturbances are still noted on the western side of the original site of the landslide.

In the image taken on October 31, 2018 (Figure 3g), the landform at the original site of the landslide appears to have been transformed again; the area of vegetation was replaced by an outcrop surface. Another transformation can be observed on the western side of the Xuyong landslide. In the 3 D image obtained by the UAV, there are obvious topographic disturbances in the upper part of the back margin of the Xuyong landslide. There is an unnatural scarp several meters in height, and clearly unnatural deposits can be found on the flat terrain immediately beneath the scarp. The distance between the artificial scarp and back margin of the Xuyong landslide is approximately 30 to 40 m. Therefore, the pre-disaster slope presents the topographic feature of a low-angle slope at the top and a high-angle slope in the lower parts. According to the above analysis of the multitemporal images, we have identified several topographic disturbances throughout the Xuyong landslide area and its surrounding regions: the Quaternary strata were removed, and the bedrock was directly exposed. In addition, the increased rainfall in this area provided conditions for the formation of a landslide hazard.

5. Post-disaster deformation observations

After the occurrence of the Xuyong landslide, ground-based radar was immediately deployed to the scene to carry out emergency observations. The observations lasted for more than 5 hours, and a total of 44 data phases were measured. The temporal sampling interval of the data was approximately 8 minutes. According to the distribution of radar echo signals, the entire landslide and artificial platform on top of the landslide showed strong echo signals due to the lack of vegetation coverage (Figure 7). Prominent and strong echo signals were also recorded from the road across the middle of the slope. In contrast, the areas with vegetation coverage on both sides of the landslide provided weak echo signals because the Ku frequency of the radar is influenced greatly by the presence of vegetation. In general, the degree of vegetation density affects the echo coherence; therefore, the denser the vegetation, the weaker the echo signal is. Finally, no

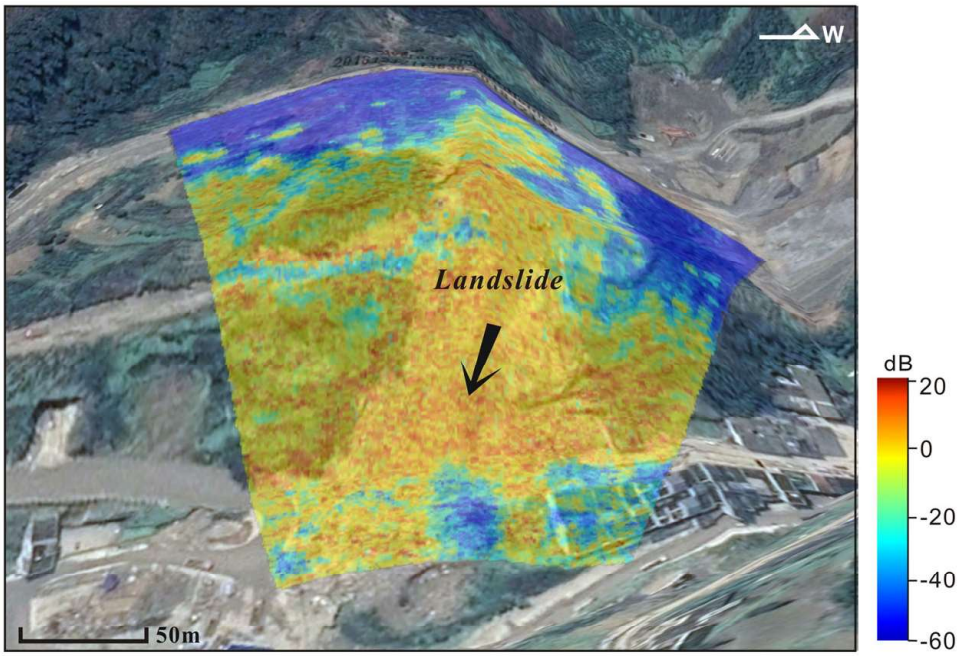

Figure 7. Distribution of echo signals measured by the ground-based radar device. The signals are superimposed onto the field photo. The white arrow denotes the slide direction of the landslide.

echo signals were recorded from either side of the landslide at the top of the slope, which is completely covered by vegetation, while the bottom of the slope still produced many echo signals because of the outcrops of bedrock, which exhibit good coherence.

Both interferometric processing and PSI timing analysis were carried out on the observed radar data to map the post-disaster deformation and analyze the spatiotemporal distribution characteristics of the landslide. Some differential interferograms generated during the processing of the ground-based radar data are shown in Figure 8. Finally, we obtained a deformation rate diagram (Figure 9a) and a cumulative deformation diagram (Figure 9b) along the radar LOS direction during the observations. The average temporal sampling interval of the data was approximately 8 minutes, and the observation lasted for more than 5 hours. A time-series deformation diagram of three representative points is also illustrated in the deformation map (Figure 10b). Figure 8a shows that there is only a small area of sliding deformation signals in the back margin of the entire landslide. In contrast, no deformation can be detected on the sliding bed or sidewalls of the landslide, indicating that most parts of the landslide are basically in a stable state. The deformation rate of point T1 along the LOS direction is 18 mm/day, and the deformation rates of points T2 and T3 are both approximately 15 mm/day. According to an analysis of the deformation characteristics of the entire landslide, it is believed that the deformation is related mainly to the flow of the surface soil and the fracturing of rocks along the back margin of the landslide. Basically, after the disaster, the entire landslide (including the sliding bed and the two sidewalls) was in a stable state; in this context, we conclude that there is a very low possibility of a secondary landslide hazard occurrence. Therefore, there is no threat to disaster rescue and relief personnel related to the post-disaster deformation of the Xuyong landslide.

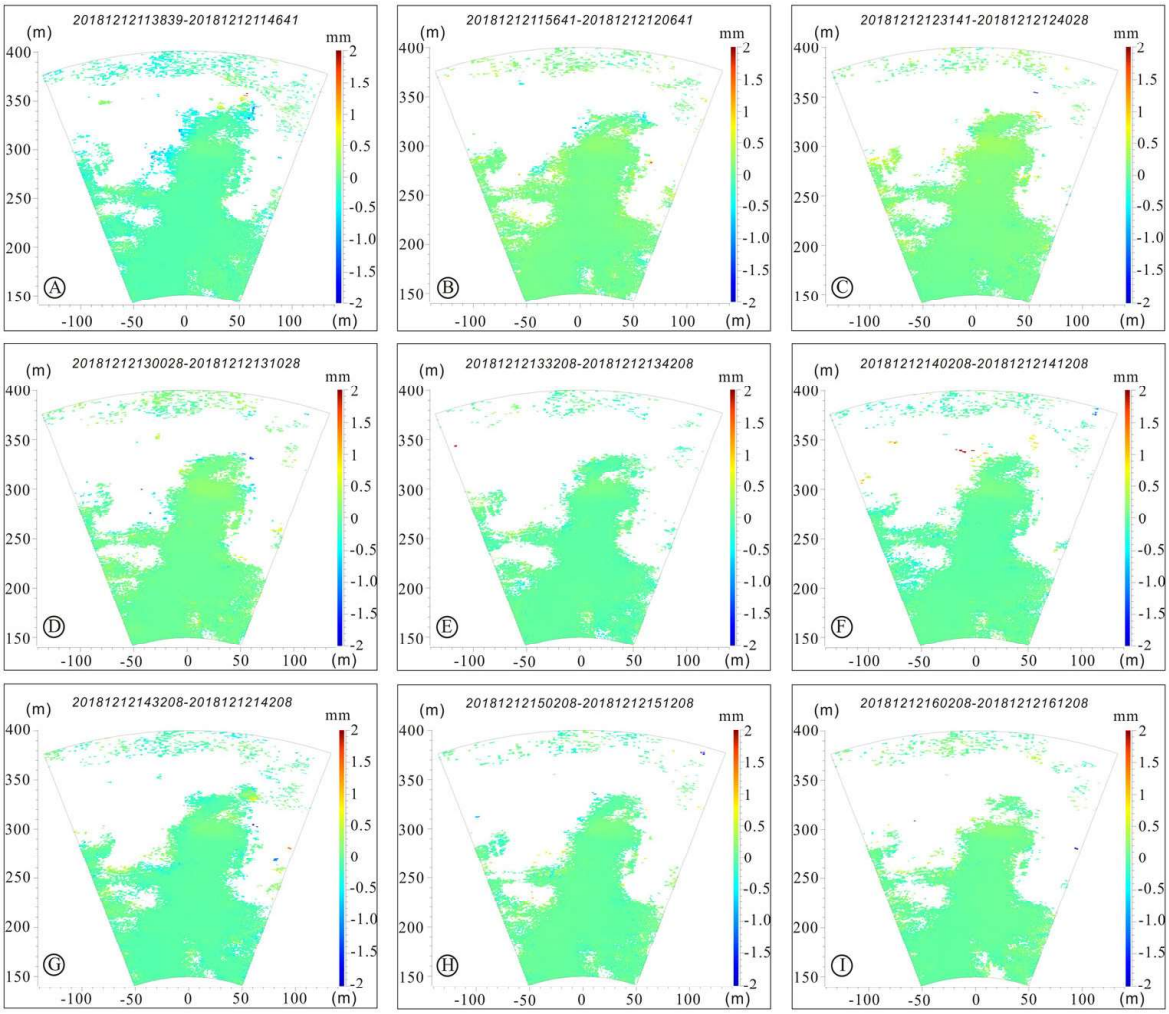

Figure 8. Examples of differential interferogram generated during the processing of ground-based radar data. The two numbers in the upper of each figure denote the observation dates of two data used to generate the differential interferogram. 20181212113839 denotes date of 11h38m39s, on December 12, 2018, 20181212113839-20181212114641 denotes differential interferogram generated between two data observed on 11h28m39s, on December 12, and 11h46m41s, on December 12. The origin point of the coordinate system is the position of the ground-based radar.

6. Discussion

6.1. Influencing factors analysis

The probability of a landslide increases when one or more influencing factors, including the rock softness, slope geometry, joint plane, shearing resistance and weathering, changes appropriately, and such changes are the foundations for the initiation of landslides (Terzaghi 1950; Varnes 1978; Popescu 1996, 2002). In terms of the natural geography and topographic conditions, slope angle is a key aspect in landslide susceptibility analysis, as a slope with a dip angle greater than 10° is prone to sliding along bedding planes (Donnarumma et al. 2013). If the lower part of the slope is steep and the upper part of the slope is gentle or if there is a flat area on the slope, the infiltration ratio of rainfall will be greater than that on a low-angle slope; this types of terrain provides favorable conditions for the formation of landslides (Liu et al. 2001; Wang et al. 2015; Wang et al. 2018). According to the field investigation, loose

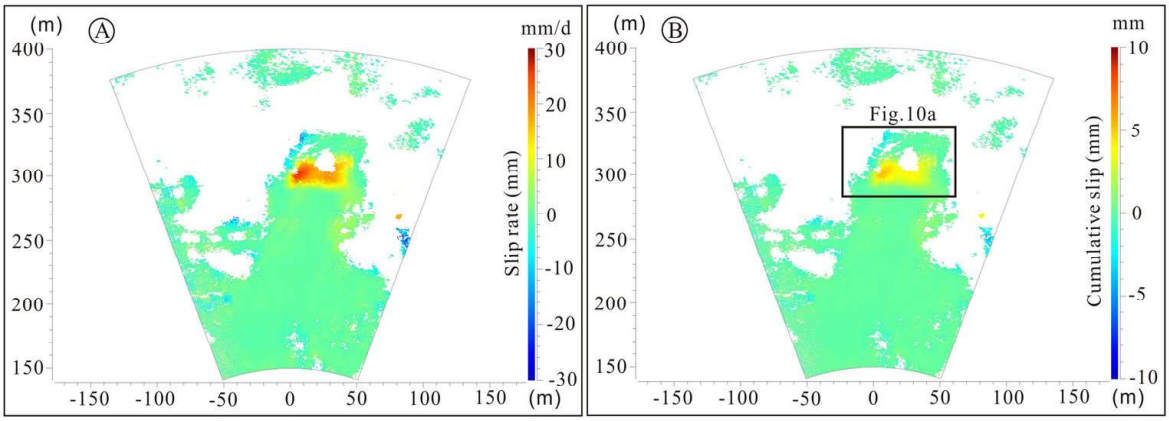

Figure 9. (1) Deformation velocity map of the surficial deformation of the landslide along the LOS direction measured by the ground-based radar device following the Xuyong landslide. (b) Cumulative slips of the surficial deformation of the landslide along the LOS direction measured by the ground-based radar device after the Xuyong landslide. The black rectangular box denotes the location of Figure 10a. The origin point of the coordinate system is the position of the ground-based radar.

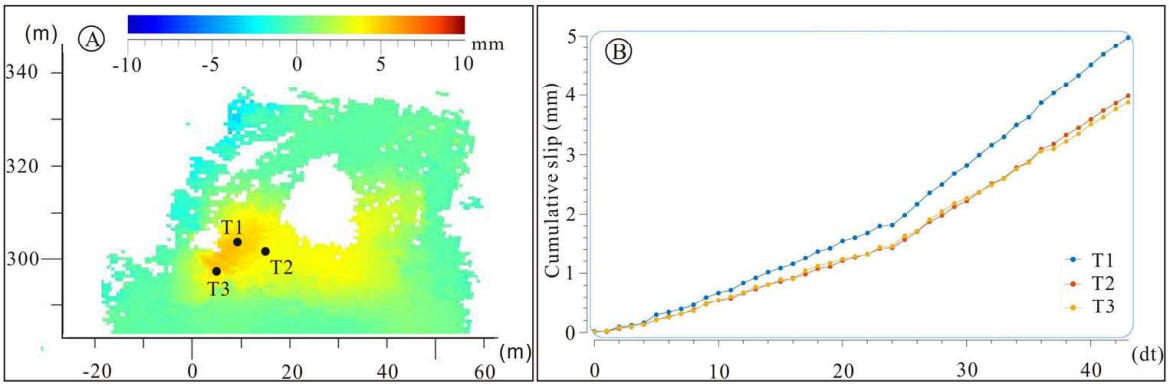

Figure 10. (a) Cumulative slips of the landslide bed along the LOS direction measured by the ground-based radar device after the Xuyong landslide. (b) Time series slips of the three points on the landslide bed along the LOS direction measured by the ground-based radar device after the Xuyong landslide. The origin point of the coordinate system is the position of the ground-based radar.

Quaternary soil and calcareous mudstone are present on top of the Xuyong landslide. Numerous thin carbonaceous layers of limestone with joint planes are also exposed in the middle part of the Xuyong landslides. Multiple sets of joint planes with different orientations are present, forming the X-shaped conjugate joints with smooth and straight planes (Figure 11a). The strata dip approximately 65° towards the NE, and the aspect of the mountain slope is approximately 45°. Therefore, the strata and the topographic slope are inclined in almost the same direction. In addition, the dip angle of the limestone layer is greater than 30°. Therefore, the slope is steep and particularly prone to instability under the long-term action of gravity because of multiple factors, including the bedding planes, steep slope, and complex joint planes.

Individual heavy rain events and long-term continuous rainfall are the main natural factors that induce geological hazards (Ding et al. 2012). Because the thin layers of limestone with joint planes are present in the slope and folded structures in this area dominate the regional tectonic background in this area, reflecting intense

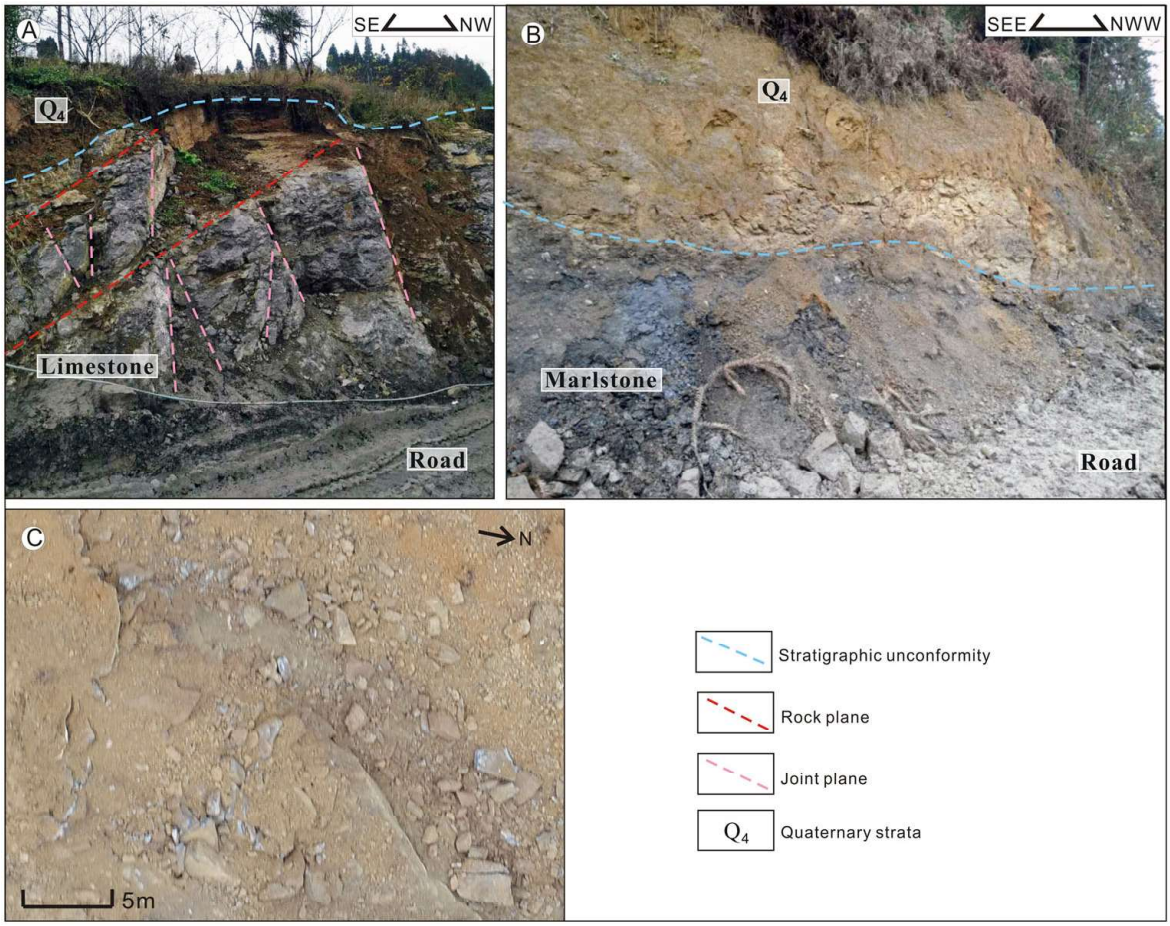

Figure 11. (a) Field photo reflecting slope lithology of the landslide in the location of Figure 4a. The blue dashed line denotes the plane of unconformity between the Quaternary strata and bedrock. The red dashed lines denote the rock planes. The pink dashed lines denote the joint planes of the limestone. The bedrock is outcropped which influences the stability of the slope. (b) Field photo reflecting the back slope lithology of the landslide in the location of Figure 4a. The blue dashed line denotes the unconformity plane between the Quaternary strata and bedrock. (c) The cracked limestone and outcropped bedrock distributed on the landslide surface revealed by the UAV image.

compressive stress, the rocks in the Xuyong area are relatively fractured. In the case of the Quaternary stratum, which is easily removed, rainfall can easily infiltrate into the bedrock layers and serve as a lubricant, facilitating sliding along bedding planes, which may have affected the stability of the slope.

In addition to natural factors, human activities, including nonstandard construction and inappropriate disturbances, are also important for inducing geological hazards (Yang et al., 2011). Topographic transformations may lead to the instability of slopes, thereby causing geological hazards. Our analysis of the multitemporal PS images before and after the landslide disaster occurred reveals that the slope of the Xuyong landslide had undergone many topographic transformations (Figure 3). The most obvious variation is the topographic damage observed at the top of the Xuyong landslide. An unnatural scarp approximately several meters in height was constructed on top of the slope and was adjacent to a large flat area; combined with the steep slope beneath this flat area, the topography was characterized by a low angle at the top of the slope and a high angle at the bottom of the slope (Figure 12). This

topographic profile is particularly detrimental to the rapid transport of precipitation along the slope during the rainy season, and rainwater can easily infiltrate into the bedrock because the surface Quaternary cover is highly fractured. Excessive rainfall infiltrating at the top of the slope may flow into the deeper bedrock, reducing the friction force between different bedrock layers and causing slope failure (Bizimana and Sonmez 2015). All of these factors provided the necessary conditions for the formation of the Xuyong landslide. The topographic transformations may have led to the unstable deformation of the slope under the action of gravity, which was also an important and unfavorable factor in the final formation of the Xuyong landslide.

6.2. Post-disaster emergency analysis

Emergency observations can track future development trends based on deformation results; hence, these observations are effective means for ensuring safety and preventing secondary dangers after landslide disasters. After occurrence of the Xuyong landslide, a ground-based GPRI-II radar instrument with the submillimeter-level accuracy was used to monitor near-real-time deformation. The GPRI-II uses a frequency-modulated continuous wave (FMCW), whereas other radar systems employ a stepped-frequency continuous wave (SFCW). Compared with SFCW systems, the GPRI-II system combines the FMCW with InSAR to monitor microdeformation of ground targets. The GPRI-II system generally uses a continuous mode to achieve the uninterrupted observation of objects and can acquire data much more quickly than other instruments.

According to the observation results, deformation only existed along the back margin of the landslide. The deformation was very low (with a maximum value of approximately 18 mm/day) and is believed to have been related to the shifting of loose soil or rocks on the surface of the slope. The bedrock and sidewalls of the landslide are basically stable. The deformation results detected by the ground-based interferometer are important in the analysis of the subsequent deformation characteristics and in the prediction of future landslide trends, both of which play important roles in safeguarding disaster rescue and relief endeavors after a landslide event.

An 8-minute sampling interval was used for the ground-based radar during the data acquisition stage in this paper. In the deformation velocity map shown in Figure 8, we can still see some incoherence effects. To reduce incoherence and atmospheric influences, the data acquisition frequency can be further improved (Li et al. 2020). Due to the impact of the radar having a single observation angle, it is impossible to fully observe the deformation features. In this context, multiangle observations could eliminate the influences of topographic shadows and improve the reflections of echo signals to capture displacements in the slope.

6.3. Applicability of different RS platforms

In recent years, different RS platforms, including satellites, UAVs and ground-based radar instruments, have been widely used in the investigation of geological hazards and in the assessment of disaster emergencies. Because the characteristics of each

platform differ from those of other platforms, different RS platforms may play different roles in different phases of landslide hazard evaluations, including the before and after landslide phases. In most cases, satellite data, including visible images and InSAR data, can be used to recognize possible hidden geological dangers and provide risk assessment through the analysis of landslide features (Delacourt et al. 2004; Hilley et al. 2004; Calabro et al. 2010; Debella-Gilo and Kaab 2012; Stumpf et al. 2014, 2017; Dong et al. 2018), including ground fissures, landslide steps, and landslide tongues, and deformation rates in the pre-disaster phase. Topographic transformations produced by human disturbances can also be recorded accurately by satellite data with the high spatial and temporal resolutions. In the case of the occurrence of the geological hazard, the UAV can be rapidly employed to capture the orthophoto images data to evaluate the influence and damaging intensities during a disaster for emergency response the first time (Casagli et al. 2017; Nikolakopoulos and Koukouvelas 2017). During this stage, satellite imagery usually cannot be captured immediately due to limitations related to satellite revisit period. In addition, both downloading of raw data from satellite and data processing need some time. During the post-disaster phase, ground-based radar is the most suitable technique for deformation observation with high precision in real time, to determine the potential of secondary landslides for the safety of emergency response (Antonello et al. 2004; Atzeni et al. 2015). In addition to its usage during the post-disaster phase, ground-based radar can also be used for identification, early warning and examination of possible geological dangers in the pre-disaster phase (Casagli et al. 2010; Atzeni et al. 2015). In conclusion, recent advances in earth observation (EO) from ground, aircraft and space have dramatically improved our ability to detect and monitor active landslides (Dai et al., 2020).

6.4. Experiences from the xuyong landslide

The Xuyong landslide is situated in the Weixin fold area, where the regional structures are very complicated and the compressive stress field is relatively intense (Deng 1965). Therefore, the strata of different geologic ages in this area are broken greatly. In addition, the bedrock dip direction is basically consistent with the slope direction, and the joint planes are extremely well-developed within the limestone (Figure 11). Besides, anthropogenic transformations of landforms may also influence stability of original slopem, potentially resulting in landslides. Although the Xuyong landslide disaster did not occur during the rainy season, the long-term precipitation in this area promoted the development of deformation to a nearly critical degree. All these factors have contributed to the occurrence of Xuyong disaster. Overall, the formation of the hidden landslide danger is affected by a combination of various factors, including the topography, tectonic environment, geological lithology, precipitation and gravity. The comprehensive sliding modes of the Xuyong landslide are illustrated in Figure 12.

According to Schuster (1995), landslide activities are expected to continue worldwide for the following reasons: (a) increased urbanization and development in landslide-prone areas, (b) continued deforestation of landslide-prone areas, and (c) increased precipitation caused by changing climatic conditions. The Xuyong landslide

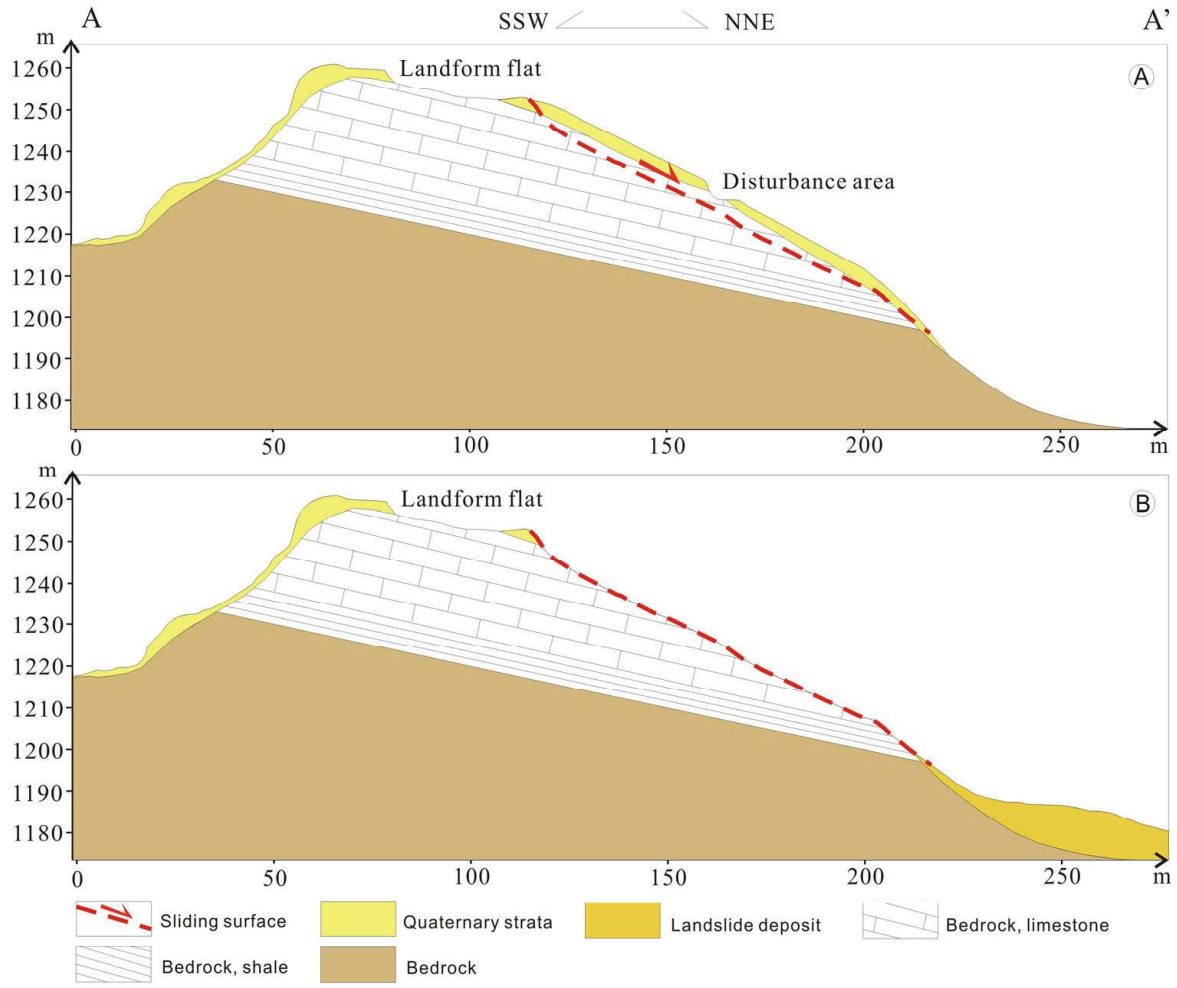

Figure 12. (a) Geological profile reflecting the sliding mode before the Xuyong landslide. (b) Geological profile reflecting the slide mode after the Xuyong landslide.

is a typical case in which a slope in a landslide-prone area was influenced by human disturbances. This landslide disaster serves as a reminder to improve efforts to assess the risks posed by geological hazards and monitor possible geological dangers. Thus, we should implement prevention measures from a variety of different perspectives. First, landslide dangers should be comprehensively prevented; this includes investigating geological environments, exploring the formation mechanisms of disasters, identifying possible landslides, providing detailed risk assessments, and enacting the dynamic monitoring of potential dangers (Bell 1999; Petley 2004; Take et al. 2004; Li et al. 2010; Hashim et al. 2018). During this process, multiplatform RS methods should be employed, including both traditional and innovative surveying techniques. Second, effective measures for avoiding geological dangers should be implemented (Bell 1999). Thus, engineering construction should avoid disturbing unstable slopes and avoid unfavorable landslide-prone areas. Finally, the real-time monitoring of potential geological dangers is necessary for their prediction and early warning (Casagli et al. 2010; Atzeni et al. 2015). Early and active avoidance or evacuation from hidden geological dangers should be carried out in cases of dangerous emergency situations. For residents living in areas of unstable geological hazards that are difficult to manage or investments that are extremely large, relocation is necessary to avoid geological disasters.

7. Conclusions

The Xuyong landslide occurred in Sichuan Province on December 9, 2018, once again serving as a warning regarding the landslide danger. It is necessary to study its formation mechanisms and influencing factors to enable the identification of potential landslide dangers under the conditions similar to those of the Xuyong landslide. Emergency observations are also important for the detection of post-disaster deformation in case of a secondary landslide disaster. Consequently, multiplatform RS technologies, including satellite images, UAV photogrammetry and ground-based radar, for different phases of the Xuyong landslide are employed in this study to clarify its formation processes, disaster features and post-disaster deformation.

Field surveying and analysis indicate that although the Xuyong landslide was a small scale landslide with a volume of approximately 35000 m^3, it was a typical dualistic soil-rock structural landslide and was the comprehensive result of many factors at multiple levels. The formation processes of the Xuyong landslide were influenced by geological structure, stratum lithology, slope topography, landform morphology, precipitation, and human disturbances. The casualties of this landslide remind us that considerable efforts should be made to recognize hidden geological dangers and monitor the sources of risk. We should investigate geological dangers from various perspectives by different methods, and effective avoidance measures are also necessary for high-risk geological dangers. After the occurrence of the Xuyong landslide disaster, immediate observations of post-disaster deformation were made to determine the possibility of a secondary landslide disaster. The results indicated the stability of the post-disaster deformation, which ensured the safety of emergency relief personnel. Our research indicates that multiple RS platforms can play important roles in different phases of landslide investigation. This study also provides a reference for the investigation and prevention of landslide dangers in environments similar to the Xuyong landslide.

Disclosure statement

Yes; Disclosure statement; No potential conflict of interest was reported by the author(s).

Acknowledgments

Many thanks to Associate Professor Yunfeng Tian, Xiuhong Hu, Ming Wen, and Tao Li, who also took part in the emergency monitoring of the Xuyong landslide. Many thanks to the editor and two anonymous reviewers for their helpful comments.

Funding

This work was supported by the Research Grants from the Institute of Crustal Dynamics, China Earthquake Administration (ZDJ2019-17 and ZDJ2017-29), and the National Natural Science Foundation of China (41772219).

References

Alizadeh M, Alizadeh E, Kotenaee SA, Shahabi H, Pour BA, Panahi M, Ahmad B, Saro L. 2018a. Social vulnerability assessment using artificial neural network (ANN) model for earthquake hazard in Tabriz city, Iran. Sustainability. 10(10):3376.

Alizadeh M, Hashim M, Alizadeh E, Shahabi H, Karami MR, Pour BA, Pradhan B, Zabihi H. 2018b. Multi-Criteria Decision Making (MCDM) Model for Seismic Vulnerability Assessment (SVA) of Urban Residential Buildings. IJGI. 7(11):444.

Alizadeh M, Ngah I, Hashim M, Pradhan B, Pour BA. 2018c. A Hybrid Analytic Network Process and Artificial Neural Network (ANP-ANN) model for urban Earthquake vulnerability assessment. Remote Sensing. 10(6):975.

Antonello G, Casagli N, Farina P, Leva D, Nico G, Sieber AJ, Tarchi D. 2004. Ground-based SAR interferometry for monitoring mass movements. Landslides. 1(1):21–28.

Atzeni C, Barla M, Pieraccini M, Antolini F. 2015. Early warning monitoring of natural and engineered slopes with Ground-Based Synthetic Aperture Radar. Rock Mech Rock Eng. 48(1):235–246.

Bell FG. 1999. Geological hazards: Their assessment, avoidance and mitigation. E & FN Spon, 11 New Fetter Lane, London EC4P4EE, United Kingdom. 1–631.

Bizimana H, Sonmez O. 2015. Landslide occurrences in the hilly areas of Rwanda, their causes and protection measures. Disaster Sci. Eng. 1(1):1–7.

Calabro M, Schmidt D, Roering J. 2010. An examination of seasonal deformation at the Portuguese bend landslide, southern California, using radar interferometry. J Geophys Res. 115(F2) F02020.doi:10.1029/2009JF001314.

Canuti P, Casagli N, Catani F, Falorni G, Farina P. 2007. Integration of Remote Sensing Techniques in Different Stages of Landslide Response. In: Sassa K, Fukuoka H, Wang F, Wang G, editors. Progress in Landslide Science. Springer-Verlag Berlin Heidelberg. 1–377.

Casagli N, Catani IF, Ventisette IC, Luzi IG. 2010. Monitoring, prediction, and early warning using ground-based radar interferometry. Landslides. 7(3):291–301.

Casagli N, Frodella W, Morelli S, Tofani V, Ciampalini A, Intrieri E, Raspini F, Rossi G, Tanteri L, Lu P. 2017. Spaceborne, UAV and ground-based remote sensing techniques for landslide mapping, monitoring and early warning. Geoenviron Disasters. 4(1):9.

Chen HQ, Xu YQ, Zhuang MG, Jiang J, Zhang N. 2011. Study on the construction of geological disaster emergency support system. Chinese J. Geol. Hazard Control. 22(4):108–111.

China geological survey. 2014. Geological map of the People's Republic of China (1: 2500000). Beijing: Map Publishing House of China.

Dai K, Peng J, Zhang Q, Wang Z, Qu T, He C, Li D, Liu J, Li Z, Xu Q, et al. 2020. Entering the Era of Earth Observation-Based Landslide Warning Systems: A novel and exciting framework. IEEE Geosci Remote Sens Mag. 8(1):136–153.

Debella-Gilo M, Kaab A. 2012. Measurement of surface displacement and deformation of mass movements using least squares matching of repeat high resolution satellite and aerial images. Remote Sensing. 4(1):43–67.

Delacourt C, Allemand P, Casson B, Vadon H. 2004. Velocity field of the La Clapière landslide measured by the correlation of aerial and QuickBird satellite images. Geophys Res Lett. 31(15)L15619. doi:10.1029/2004GL020193

Deng QD, Zhang PZ, Ran YK, Yang XP, Min W, Chu QZ. 2002. Basic characteristics of active tectonics of China. Science China (Series D). 32:1020–1030.

Deng YG. 1965. Primary discussion of the originations of the early to middle Triassic breccia and its relationship with the salt deposits in southeastern Sichuan. Geological Review. 23(6): 502–509.

Ding W, Yang Q, Wang A, Gao Y, Yang X, Li Q. 2012. Study on and application of geological hazards meteorological early-warning in the loess area: a study in Jingchuan County in eastern Gansu province of China. Journal of Geo-Information Science. 13(6):811–818.

Dong J, Zhang L, Li M, Yu Y, Liao M, Gong J, Luo H. 2018. Measuring precursory movements of the recent Xinmo landslide in Mao County, China with Sentinel-1 and ALOS-2 PALSAR-2 datasets. Landslides. 15(1):135–144.

Donnarumma A, Revellino P, Grelle G, Guadagno FM. 2013. Slope Angle as Indicator Parameter of Landslide Susceptibility in a Geologically Complex Area. In: Margottini C, Canuti P, Sassa K, editors. Landslide Science and Practice Springer-Verlag Berlin Heidelberg; p. 425–433..

Fan X, Xu Q, Scaringi G, Dai L, Li W, Dong X, Zhu X, Pei X, Dai K, Havenith H-B. 2017. Failure mechanism and kinematics of the deadly June 24th 2017 Xinmo landslide, Maoxian, Sichuan, China. Landslides. 14(6):2129–2146.

Hashim M, Misbari S, Pour BA. 2018. Landslide mapping and assessment by integrating Landsat-8, PALSAR-2 and GIS techniques: a case study from Kelantan state, peninsular Malysia. J Indian Soc Remote Sens. 46(2):233–248.

Hilley G, Burgmann R, Ferretti A, Novali F, Rocca F. 2004. Dynamics of slowmoving landslides from permanent scatterer analysis. Sci. 304(5679):1952–1955.

Intrieri E, Gigli G. 2016. Landslide forecasting and factors influencing predictability. Nat Hazards Earth Syst Sci. 16(12):2501–2510.

Iverson RM. 2000. Landslide triggering by rain infiltration. Water Resour Res. 36(7): 1897–1910.

Lacroix P, Berthier E, Maquerhua ET. 2015. Earthquake-driven acceleration of slow moving landslides in the Colca Valley, Peru, detected from Pléiades images. Remote Sens. Environ. 165:148–158.

Li BQ, Li YS, Jiang WL, Cai JW, Gan J. 2019. Research and Application of Slope Dynamic Monitoring Based on Ground-Based Real Aperture Radar. Geomatics Inf. Sci. Wuhan University. 44(7): 1093–1098.

Li YS, Jiao QS, Hu XH, Li ZL, Li BQ, Zhang JF, Jiang WL, Luo Y, Li Q, Ba RJ. 2020. Detecting the slope movement after the 2018 Baige landslides based on ground-based and space-borne radar observations. Int. J Appl Earth Obs. Geoinf. 84:101949.

Li YS, Zhang JF, Li ZH, Luo Y. 2013. Land subsidence in Beijing city from InSAR time aeries analysis with small baseline subset. Geomatics Inf. Sci. Wuhan University. 38(11): 1374–1377.

Li Z, Huang H, Nadim F, Xue Y. 2010. Quantitative Risk Assessment of Cut-Slope Projects under Construction. J Geotech Geoenviron Eng. 136(12):1644–1654.

Liang X, Ye X, Zhang JH, Shu HL. 2011. Reservoir forming conditions and favorable exploration zones of shale gas in the Weixin Sag, Dianqianbei Depression. Pet Explor Dev. 38(6): 693–699.

Liu CZ. 2006. Basic problem on emergency disposition of abrust heavy geological disaster. J Nat. Disaster. 15(3):24–30.

Liu JG, Lei TW, Xia WS, Pan YH, Zhang WQ. 2001. Processes and model of rainfall infiltration on slope and treated with PAM. J Soil Water Conserv. 15(4):51–54.

Monserrat O, Crosetto M, Luzi G. 2014. A review of ground-based SAR interferometry for deformation measurement. ISPRS J Photogramm Remote Sens. 93:40–48.

National Geological Archives of China. 2013. Regional hydrogeology survey report of Xuyong in scale of 1: 200, 000. Beijing: Geological Publishing House.

Nikolakopoulos KG, Koukouvelas IK. 2017. Emergency response to landslide using GNSS measurements and UAV. Earth Resources and Environmental Remote Sensing/Gis Applications.

Noferini L, Pieraccini M, Mecatti D, Luzi G, Atzeni C, Tamburini A, Broccolato M. 2005. Permanent scatterers analysis for atmospheric correction in ground-based SAR interferometry. IEEE Trans Geosci Remote Sensing. 43(7):1459–1471.

Noferini L, Pieraccini M, Mecatti D, Macaluso G, Atzeni C, Mantovani M, Marcato G, Pasuto A, Silvano S, Tagliavini F. 2007. Using GB-SAR technique to monitor slow moving landslide. Eng Geol. 95(3-4):88–98.

Osmanoğlu B, Dixon TH, Wdowinski S, Cabral-Cano E, Jiang Y. 2011. Mexico city subsidence observed with persistent scatterer InSAR. Int J Appl Earth Obs Geoinf. 13(1):1–12.
Petley DN. 2004. The evolution of slope failures: mechanisms of rupture propagation. Nat Hazards Earth Syst Sci. 4(1):147–152.
Pieraccini M, Casagli N, Luzi G, Tarchi D, Mecatti D, Noferini L, Atzeni C. 2003. Landslide Monitoring by Ground-Based Radar Interferometry: a field test in Valdarno (Italy). Int J Remote Sens. 24(6):1385–1391.
Popescu ME. 1996. From landslide causes to landslide remediation. Special Lecture. Proc.7th Int. Symp. On Landslides Trondheim. 1:75–96.
Popescu ME. 2002. Landslide causal factors and landslide remediatial options. In 3rd International Conference on Landslides. Citeseer: Slope Stability and Safety of Infra-Structures.
Pour BA, Hashim M. 2017. Application of Landsat-8 and ALOS-2 data for structural and landslide hazard mapping in Kelantan, Malaysia. Nat Hazards Earth Syst Sci. 17(7):1285–1303.
Schuster RL. 1995. Socio-economic significance of landslides. In: Turner AK, Schuster RL, editors. Landslides, Invest Mitigation. Transp Res Board Spec. Report 247. Washington DC: National Academy of Sciences. p. 12–35.
Shi Y, Huang W, Ye H, Ruan C, Xing N, Geng Y, Dong Y, Peng D. 2018. Partial least square discriminant analysis based on normalized two-stage vegetation indices for mapping damage from rice diseases using planet scope datasets. Sensors. 18(6):1901.
Smith R, Knight R, Fendorf S. 2018. Over pumping leads to California groundwater arsenic threat. Nature Communication. 9:2089.
Stumpf A, Malet JP, Allemand P, Ulrich P. 2014. Surface reconstruction and landslide displacement measurements with Pléiades satellite images. ISPRS J. Photogramm. Remote. Sensing. 95:1–12.
Stumpf A, Malet JP, Delacourt C. 2017. Correlation of satellite image time-series for the detection and monitoring of slow-moving landslides. Remote Sens. Environ. 189:40–55.
Sun H, Zhao Y, Shang Y, Zhong J. 2013. Field measurement and failure forecast during the remediation of a failed cut slope. Environ Earth Sci. 69(7):2179–2187.
Take WA, Bolton MD, Wong PC, Yeung FJ. 2004. Evaluation of landslide triggering mechanisms in model fill slopes. Landslides. 1(3):173–184.
Tarchi D, Casagli N, Fanti R, Leva D, Luzi G, Pasuto A, Pieraccini M, Silvano S. 2003a. Landslide monitoring by using ground-based SAR interferometry: an example of application to the Tessina landslide in Italy. Eng Geol. 68(1-2):15–30.
Tarchi D, Casagli N, Moretti S, Leva D, Sieber AJ. 2003b. Monitoring landslide displacements by using ground-based synthetic aperture radar interferometry: Application to the Ruinon landslide in the Italian Alps. J Geophys Res. 108(B8):2387.
Terzaghi K. 1950. Mechanisms of landslides. Geological Society of America. Engineering Geology, Berkley, p. 83–123
Varnes DJ. 1978. Slope movements and types and processes. Landslides analysis and control. Transp Res. Board Spec. Rep. 176:11–33.
Ventisette CD, Intrieri E, Luzi G, Casagli N, Fanti R, Leva D. 2011. Using ground based radar interferometry during emergency: the case of the A3 motorway (Calabria Region, Italy) threatened by a landslide. Nat Hazards Earth Syst Sci. 11(9):2483–2495.
Wang H, Wright TJ, Biggs J. 2009. Interseismic slip rate of the northwestern Xianshuihe fault from InSAR data. Geophys Res Lett. 36(3):n/a–145.
Wang RH, Zhou HQ, Liu QY. 2018. Failure modes of key blocks in high slope with steep downward soil. Journal of Water Resources and Architectural Engineering. 16(03):165–169.
Wang ZB, Yu B, Zhu YB, Ma M, Yi W. 2015. Preliminary study on the slope surface rainfall infiltration of rain intensity and topography (slope gentle in the upper and steep in the lower). Science Technology and Engineering. 15(02):314–317.
Werner C, Wiesmann A, Strozzi T, Kos A, Wegmiuler U. 2012. The GPRI multi-mode differential interferometric radar for ground-based observations. Synthetic Aperture Radar, EUSAR. 9th European Conference on. VDE.

Yan G, Yin Y, Huang B, Zhang ZH, Zhu SN. 2019. Formation mechanism and characteristics of the Jinjiling landslide in Wushan in the Three Gorges Reservoir region, China. Landslides. 16(11):2087–2101.

Yang YQ, Hu JF, Xi MH. 2011. Analysis of influence factors of debris flow disaster in zhouqu based on grey relevance method. Journal of Natural Disasters. 20(3): 139–144.

Yin Y, Xing A, Wang G, Feng Z, Li B, Jiang Y. 2016. Experimental and numerical investigations of a catastrophic long-runout landslide in Zhenxiong, Yunnan, southwestern China. Landslides. 14(2):1–11.

Zhao R, Xu M, Fan CC, Wang CT. 2015. Discussion on the characteristics of Karst development and influence factors in Gulin-Xuyong area of southern Sichuan. Research of Soil and Water Conservation. 22(2):316–319.